Available online at www.sciencedirect.com
ScienceDirect
Trans. Nonferrous Met. Soc. China 31(2021) 1205−1216
Transactions of Nonferrous Metals Society of China
www.tnmsc.cn

In situ thermomechanical processing to avoid grain boundary precipitation and strength-ductility loss of age hardening alloys

Yong-hao ZHAO

Nano and Heterogeneous Materials Center, School of Materials Science and Engineering, Nanjing University of Science and Technology, Nanjing 210094, China

Received 4 June 2020; accepted 22 December 2020

Abstract: To avoid grain boundary (GB) precipitation during aging, a new strategy of in situ thermomechanical processing for age hardening alloys was proposed. Specifically, high-density nanoscale precipitates were introduced into ultrafine grain (UFG) interiors of 7075Al alloy by equal-channel-angular (ECAP) processing at 250 °C for 8 passes, thus avoiding GB precipitation. Tensile test results indicated that the UFG 7075Al alloy exhibits superior mechanical properties (yield strength of 350 MPa, ultimate tensile strength of 500 MPa, uniform elongation of 18% and tensile ductility of 19%) compared with the UFG 1050Al counterpart (yield strength of 170 MPa, ultimate tensile strength of 180 MPa, uniform elongation of 2.5% and tensile ductility of 7%). Fracture surface morphology studies revealed numerous homogeneous micro shear bands in necking shrinkage areas of both UFG 7075Al and 1050Al alloys, which are controlled by cooperative GB sliding. Moreover, the introduction of nanoscale precipitates in UFG 7075Al matrix weakened the tendency of shear fracture, resulting in a higher tensile ductility and more homogeneous deformation. Different from the GB precipitation during postmortem aging, in situ thermomechanical treatment dynamically formed GBs after precipitation, thus avoiding precipitation on GBs.

Key words: age hardening alloys; strength; fracture elongation; grain boundary precipitation; in situ thermomechanical processing

1 Introduction

Bulk nanostructured (10−100 nm in grain size, NS) and/or ultrafine grained (100−1000 nm in grain size, UFG) materials, with typically 5−10 times higher strength than that of conventional materials of similar composition, have been widely investigated over past few decades [1−3]. However, their high strength is often achieved at the expense of ductility due to their low strain hardening capability, which limits the widespread applications of the NS and UFG materials [4−8]. Up to now, various strategies and techniques have been proposed and investigated in an effort to improve the low ductility of the NS materials by tailoring their microstructures [9,10]. Detailed strategies include eliminating processing artifacts [11], bi-modal and multimodal grain size distributions [12], nanoscale second-phase precipitates/particles dispersed in NS and/or UFG grains [13−15], nanoscale twin boundaries [16], transformation-induced-plasticity (TRIP) and twinning-induced-plasticity (TWIP) effects [17], lowering dislocation density [18], deforming at low temperature or high strain rate [19−21], heterogeneous structure and back-stress effect [22,23]. Among these strategies, introducing nanoscale second-phase precipitates/particles has been found to be broadly applicable to age hardening alloys.

The idea of introducing nanoscale second-phase precipitates/particles to regain the strain

Corresponding author: Yong-hao ZHAO, Tel: +86-18915971789, E-mail: yhzhao@njust.edu.cn
DOI: 10.1016/S1003-6326(21)65572-3

hardening and ductility of the UFG metals was first proposed by KOCH in 2003 [24]. The NS and UFG materials do not exhibit high strain hardening or ductility because dislocations are emitted from and annihilated at grain boundaries (GBs) without accumulation in the grain interior. In other words, the NS or UFG grains have no enough room for dislocation propagation and interactions. However, if nanoscale second-phase particles are introduced in the grain interior, dislocations will be forced to accumulate when they intersect or by-pass second-phase particles. The accumulation of dislocations should lead to strain hardening and consequently higher tensile ductility. To verify this hypothesis, we used age hardening 7000Al alloy as a model material. The sample was first solution-treated and then rolled at liquid nitrogen temperature to form the UFG grains. Subsequent aging introduced a large number of nano-precipitates and enhanced the strain hardening rate and tensile ductility. High-resolution electron microscopy (HREM) verified that the second-phase precipitates indeed acted to block and accumulate dislocations [13]. Moreover, this approach involving the precipitation of second-phases for enhancing the strain hardening and tensile ductility of the UFG materials has been reported by several other groups with various degrees of success [25−29]. Using a similar argument, nanosized second-phase particles were also introduced into the UFG microstructures by powder metallurgy [30−32] or breakdown of coarse second-phase particles using severe plastic deformation [33,34]. For example, nanoparticle La_2O_3 was introduced into UFG Mo matrix, and yield strength over 800 MPa and tensile ductility over 35% were achieved [15]. More recently, nanoscale precipitates or clusters with high density have been revealed in FeNiAlMo maraging steel and FeCoNiAlTi high-entropy alloys [35,36], which significantly enhanced the yield strength over 2 and 1 GPa while still remained 8% and 50% tensile ductility, respectively.

It should be noted that, the postmortem aging after deformation usually simultaneously introduces precipitates at the GBs except in the grain interiors, and the GB precipitation is harmful to tensile ductility. In 2012, WEN et al [37] employed in situ thermomechanical treatment to produce UFG Cu alloy by equal-channel-angular pressing (ECAP) at 200 °C. They found that the mechanism governing microstructural refinement is continuous dynamic recrystallization (CDRX). This former work inspired us to employ the in situ thermo-mechanical treatment to refine the initial coarse grains of age hardening alloys, and at the same time introduce nanoscale precipitates in the grain interiors only.

In this work, in order to avoid GB precipitation during postmortem aging, we proposed a new processing strategy of in situ thermomechanical processing for age hardening alloys, and verified the effectiveness of such a strategy in precipitation strengthened UFG 7075Al alloy. This strategy may be applicable to optimize strength and ductility of different age hardening alloys by avoiding GB precipitation.

2 Experimental

2.1 Materials and ECAP processing

Commercial 1050Al and 7075Al bars were used for ECAP experiments. Chemical compositions were analyzed in Luvak Inc. (Boylston, MA) and listed in Tables 1 and 2, respectively. The chemical composition analysis method was direct current plasma emission spectroscopy (ASTME−1097−03). The main alloying elements are Fe and Si for 1050Al alloy, and Zn, Mg and Cu for 7075Al alloy. Before ECAP, the 7075Al bars were treated at 480 °C for 5 h to form a homogeneous solid solution and then quenched to room temperature in water. The quenched 7075Al bars were immediately placed in an ECAP die and heated up to 250 °C with a heating rate of 20 °C/min, and then deformed by route Bc, in which the sample was rotated by 90° in the same direction between each pass, for 8 passes. The 1050Al bars were processed using ECAP at ambient temperature by route Bc for 8 passes. The ECAP die has an L-shaped channel with an intersecting angle of 90° and an outer-arc

Table 1 Chemical compositions of 1050Al alloy (wt.%)

Si	Fe	Cu	Mn	Mg	Zn	Ti	Al
0.08	0.31	0.003	0.036	0.004	0.009	0.008	99.5

Table 2 Chemical compositions of 7075Al alloy (wt.%)

Zn	Mg	Cu	Fe	Si	Mg	Cr	Ti	Others	Al
5.80	2.50	1.55	0.21	0.098	0.050	0.20	0.025	<0.15	Bal.

angle of 45°. An effective strain of approximately 1 was imposed per ECAP pass.

2.2 Tensile testing

Flat dog-bone tensile specimens with gauge dimensions of 1 mm × 2 mm × 15 mm for 7075Al alloy and 1 mm × 2 mm × 10 mm for 1050Al alloy were sectioned by electrical discharge machining (EDM). The gauge axis of tensile specimens was parallel to the ECAP extrusion direction. All tensile specimens were polished before testing using a diamond suspension with a particle size of 0.25 μm. Uniaxial tensile tests were performed at room temperature on an Instron 8801 universal testing machine (UTM) using Bluehill 2 software with an initial quasi-static strain rate of 10^{-3} s^{-1}. The strain was measured using a standard non-contacting video extensometer with a 100 mm field-of-view lens.

2.3 Microstructural characterization

Microstructures of the 7075Al and 1050Al samples after ECAP were characterized using transmission electron microscopy (TEM) on a Philips CM12 microscope operated at 100 kV. 7075Al TEM specimens were prepared by first mechanically grinding the samples to a thickness of 20−30 μm, then dimpling to a thickness of about 10 μm, and finally ion-milling to a thickness of electron transparency using a Gatan Precision Ion Milling System with an Ar^+ accelerating voltage of 4 kV and a temperature below 35 °C. 1050Al TEM specimens were prepared by first polishing the samples into thin foils with thicknesses of about 50 μm, and then twin-jet electro-polishing in a solution of 25 vol.% nitric acid and 75 vol.% methanol for 2 min at a voltage of 15 V and a temperature of −35 °C.

The HREM was performed on a JOEL 2500 TEM operating at 200 kV. The fracture surface and morphology were imaged by an FEI-XL30 SFEG scanning electron microscopy (SEM) using a 25 kV beam.

3 Results

3.1 Microstructures

As shown in Fig. 1, the ECAP-processed UFG 7075Al alloy is composed of equiaxed grains with an average grain size of about 800 nm. From the continuous ring-like selected-area electron diffraction (SAED) pattern of a circle area with a diameter of 5.4 μm at the upper left corner of Fig. 1(a), one can conclude that the grains are randomly oriented due to the large imposed ECAP deformation strain. Moreover, spherical and cylindrical-shaped precipitates, with diameters of several ten nanometers and interparticle distances ranging from several ten to several hundred nanometers, were observed in the grain interiors but very seldom at the GBs. Based on the insets of the SAED pattern at the upper right corner of Fig. 1(a) (as pointed by white arrow) and HREM image of the precipitate−Al interface at the lower right corner of Fig. 1(d), these precipitates have been identified as primarily the non-coherent stable η phase. Based on the published results [38], ECAP altered the η phase orientation and atomic configuration as well as the interfacial energy with the Al matrix, such that the initially cylindrical-shaped η phase adopted isotropic growth morphology and evolved into equiaxed particles.

Dislocation density in most grains was low and some dislocations were pinned by the precipitates, as highlighted by red arrows in Fig. 1. In addition, low-angle GBs formed by polygonized dislocation walls (PDWs) were frequently observed, as shown in Figs. 1(b−d) highlighted by blue arrows. It has been reported that the UFG materials processed at elevated temperatures have a higher fraction of low-angle GBs, in comparison with those processed at room temperature [37]. A possible explanation for this observation may be the kinetic recovery of dislocations into dislocation walls at higher temperatures. This is consistent with the low dislocation density observed herein, and hence only pinned dislocations remained after deformation. Moreover, Fig. 1(b) shows an inclined GB that is not vertical or edge-on to the paper plane, as pointed by green arrows. Equal thickness stripes can be discerned, from which GBs free of precipitates were further confirmed.

The UFG 1050Al counterpart is composed of equiaxed grains with an average size of 700 nm. From the continuous ring-like SAED pattern in Fig. 2(a), one can conclude that the grains are randomly oriented due to the large imposed ECAP deformation strain. Most of grains are free of dislocations and possess large misorientations from their surrounding grains, suggesting that they were

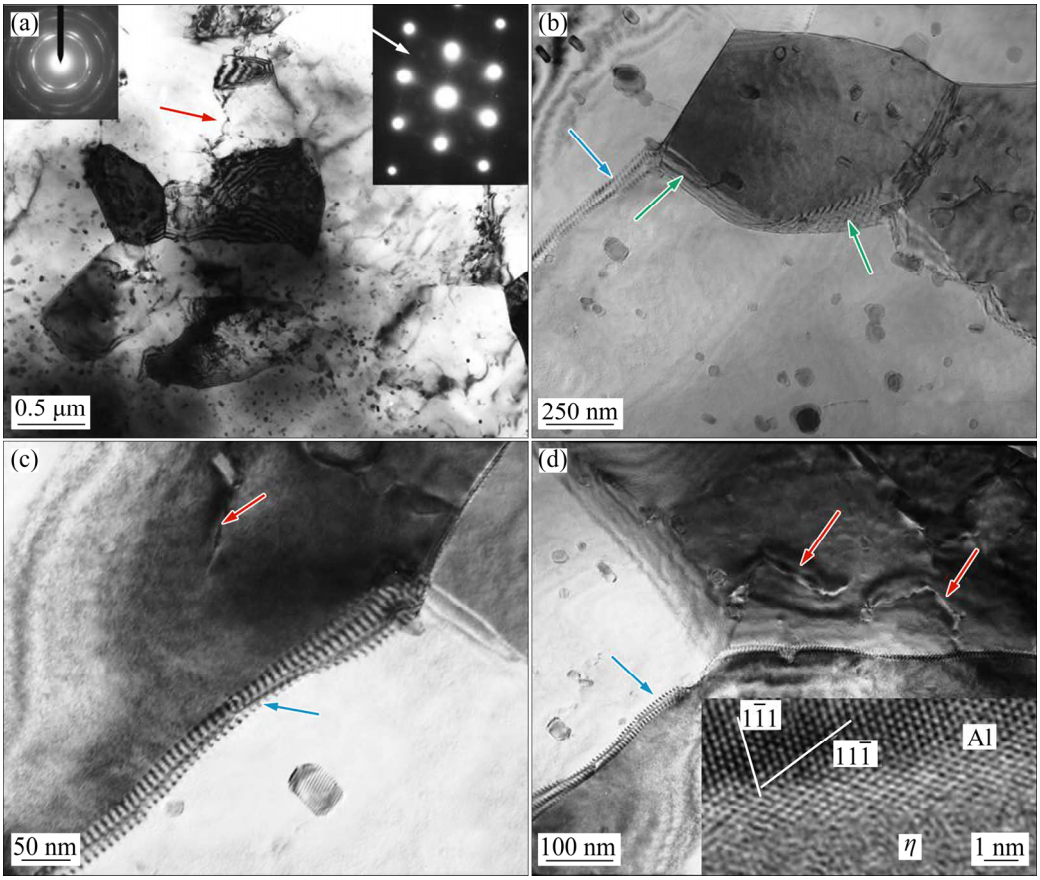

Fig. 1 Bright-field low-magnification TEM image of UFG 7075Al alloy with insets of SAED patterns (a) and magnified TEM images with low-angle GBs (pointed by blue arrows), inclined GB (pointed by green arrows) and dislocations pinned by precipitates (pointed by red arrows) (b−d) (inset at lower right corner in (d) is HREM image taken at η-precipitate−Al interface)

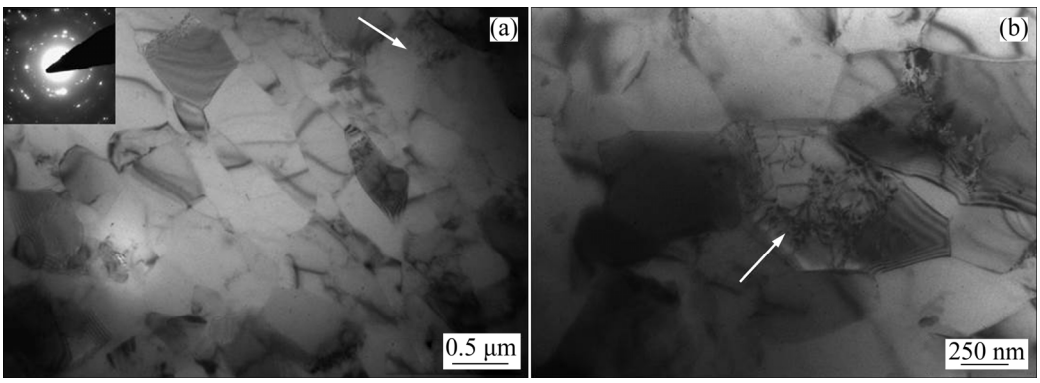

Fig. 2 TEM images of UFG 1050Al alloy (Dislocation tangling was pointed out by white arrows): (a) Lower magnification; (b) Higher magnification

formed as a result of dynamic recrystallization during ECAP processing at room temperature [39]. In Ref. [40], it was reported that the restoration occurred to some degree during ECAP processes, which can be attributed to adiabatic heating and accumulated strain because of severe plastic deformation. Moreover, few grains were observed to contain statistically stored dislocations (such as entangled dislocations, dislocation forests and discrete single dislocations) as marked by the white arrows in Fig. 2.

3.2 Tensile testing results

The representative engineering stress−strain curves of the UFG 7075Al and 1050Al alloys are compared in Fig. 3. The UFG 7075Al sample has a

yield strength of 350 MPa, ultimate tensile strength of 500 MPa, uniform elongation of 18% and tensile ductility of 19%. While the UFG Al counterpart only has the yield strength of 170 MPa, ultimate tensile strength of 180 MPa, uniform elongation of 2.5% and tensile ductility of 7% (Table 3). For the UFG Al alloy, the necking phenomenon occurred immediately after yielding. Such a necking instability is due to the lack of strain strengthening and dislocation storage after severe plastic deformation. Introducing nanoscale precipitates to the UFG 7075Al alloy enhanced both yield strength and tensile ductility by enhancing the strain hardening capability. These results indicated that the strain hardening has been remarkably regained due to the impeding effect of nanoscale precipitates to dislocations.

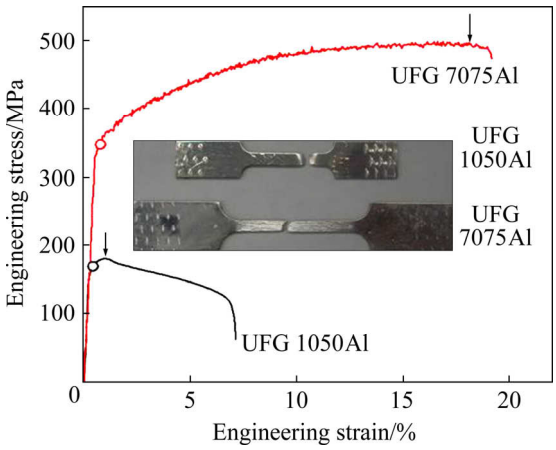

Fig. 3 Tensile engineering stress−strain curves of UFG 7075Al and 1050Al alloys (The inset shows fractured tensile specimens with dimensions of 1 mm × 2 mm × 15 mm for 7075Al specimen and 1 mm × 2 mm × 10 mm for 1050Al specimen)

Table 3 Yield strength $\sigma_{0.2}$, ultimate tensile strength σ_{UTS}, uniform elongation ε_{ue}, tensile ductility ε_{ef}, shear fracture angle θ and area reduction of fracture surface A of UFG 7075Al and 1050Al samples

Sample	$\sigma_{0.2}$/ MPa	σ_{UTS}/ MPa	ε_{ue}/ %	ε_{ef}/ %	θ/ (°)	A/ %
1050Al	170	180	2.5	7	52	40
7075Al	350	500	18	19	58	35

It should be noted that the evidently larger ductility of the UFG 7075Al than that of the UFG 1050Al was not caused by their differences in dimensions of tensile specimens, although our related work indicated that the tensile curve is closely related with the tensile specimen size [41,42]. Based on the results in Refs. [41,42], a smaller gauge length of tensile specimen corresponds to a larger tensile ductility. The gauge length of the UFG 7075Al alloys is 15 mm, which is larger than that of the UFG 1050Al alloy (10 mm). Therefore, the larger tensile ductility of the UFG 7075Al alloy was not caused by its larger gauge length.

3.3 Fracture modes and deformation mechanisms

To further understand the tensile behavior and establish the relationship between microstructures and mechanical properties, we studied the fracture mode and surface morphology using SEM. Figure 4 shows SEM images of the macro- and micro-scale fracture surfaces of the UFG 7075Al and 1050Al samples. From the macro-scale SEM image (Fig. 4(a)), the fracture surface of the UFG 7075Al alloy is irregular, with a high concentration of uneven concave and protrusion. It is evident that the material fractured in a ductile manner, as evidenced by the homogeneously distributed honeycomb-like dimples and a large area reduction of fracture surface of 35%. Careful inspection showed that the dimple size ranged from 100 to 500 nm, which is consistent with the interparticle distance of the η precipitates as determined based on the TEM image in Fig. 1. Moreover, spherical particles are observed at the bottom of the dimples, as pointed out by red arrows in Fig. 4(b), which have a similar size and morphology as the η precipitates observed via TEM. These results suggest that during tension, the η phase resisted deformation and detached from the matrix.

The UFG 1050Al sample fractured also via a ductile mechanism with a large area reduction of fracture surface of 40% and numerous dimples over the entire fracture surface. From the micro- scale SEM image in Fig. 4(d), homogeneously distributed honeycomb-like dimples having an average size of several micrometers were observed. Moreover, the dimples are elongated due to void nucleation and subsequent coalescence via shear fracture.

Figures 5(a, b) show the macro- and micro-scale fracture SEM images from face-view of the UFG 7075Al and 1050Al samples, respectively. Careful observation on the sample surface revealed numerous localized plastic deformation markings or

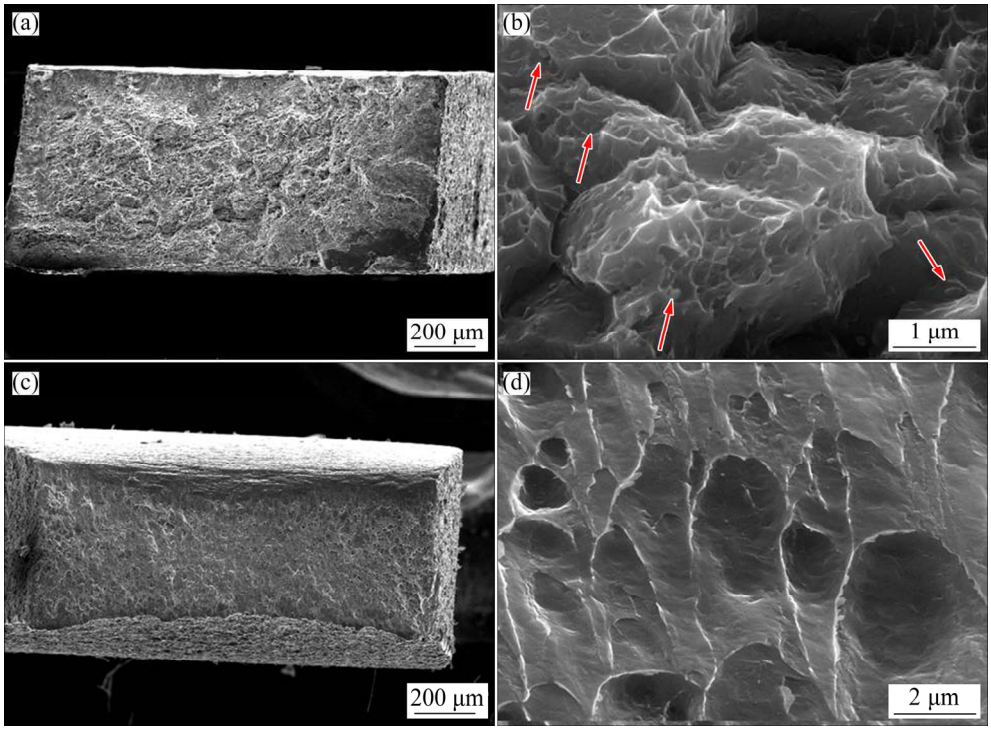

Fig. 4 SEM images of fracture surfaces of UFG 7075Al (a, b) and 1050Al (c, d) samples: (a, c) Lower magnification; (b, d) Higher magnification

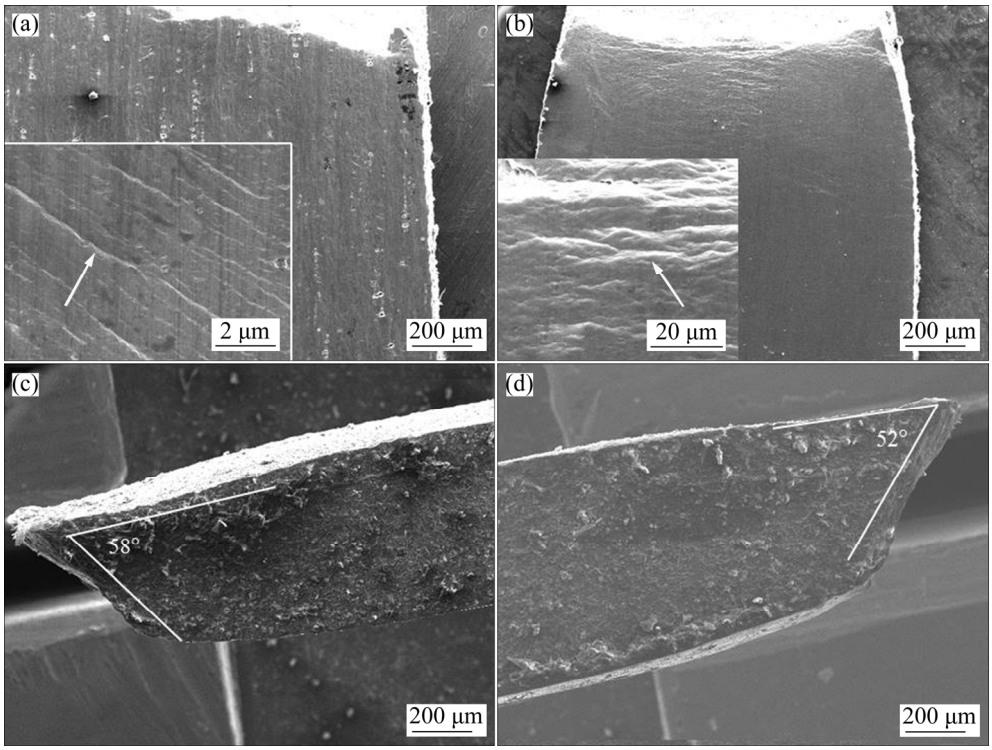

Fig. 5 Face-view SEM images of UFG 7075Al (a) and 1050Al (b) samples (Insets are high-magnification images near necking) and side-view SEM images of UFG 7075Al (c) and 1050Al (d) samples

traces parallel with each other near the fracture edge within the necking zones, as shown in the insets of Figs. 5(a, b) and pointed out by the white arrows. Several published studies reported similar deformation traces in UFG Al alloys [39,43,44], 6082 Al alloys [45], Ni and Cu alloys [46], which

were described as microscopic or mesoscopic shear bands or shear planes. The distances between shear bands vary from several micrometers to several ten micrometers, and the lengths of the shear bands extend from several micrometers to several hundred micrometers. The shear bands are much coarser in 1050Al samples, as shown in Fig. 5(b). This result suggests that the formation of the high density of fine shear bands in 7075Al alloy may have enhanced the plastic deformation capability and overall tensile ductility.

Figures 5(c, d) show the SEM images from side-view of the UFG 7075Al and 1050Al alloys, respectively. Both samples failed in a shear fracture mode with a shear fracture angle θ (the angle between the fracture surface and tension axis) of about 58° and 52°, respectively. The shear fracture can be attributed to the nanostructures, which resulted in a decreased ratio of the average critical normal fracture stress to shear fracture stress [47,48].

4 Discussion

4.1 Tensile ductility

For engineering structural materials, it is ideal to simultaneously possess both high ductility for attaining higher toughness, formability and deformability, and high strength for carrying more load. Unfortunately, strength and ductility of a material are generally seldom co-existing simultaneously and exclusive/trade-off with each other. That is, strength and ductility are consuming each other. Strengthening is accompanied with the expense of plasticity, and enhancing ductility has to lower or sacrifice the yield strength. This is the well-known so-called strength−ductility paradox, which is like either end of a teeterboard, i.e., elevating one has to lower the other.

The strength−ductility paradox exists universally in nature and is seldom broken [1−10]. For metals and alloys, dislocation slip-dominated plastic deformation determines strength−ductility paradox. Conventional strengthening mechanisms including the grain refinement and deformation routinely increase the yield strength by increasing the critical shear stress for slip initiation, while the ductility is related not only with the dislocation nucleation, but also more closely with slip kinetics, and is weakened more or less by the traditional strengthening mechanisms. Deformation-induced GBs and dislocation cells impeded the dislocation slip and multiplication, and therefore reduced the ductility.

Based on Hart's theory [49], during tension necking instability occurs when

$$\Theta \le \sigma(1-m) \tag{1}$$

where Θ ($=\partial\sigma/\partial\varepsilon$) is strain hardening rate, m ($=\partial\ln\sigma/\partial\ln\dot{\varepsilon}$) is strain rate sensitivity, and σ, ε and $\dot{\varepsilon}$ are true stress, true strain and strain rate, respectively. From Eq. (1), one can see that both high strain hardening rate and strain rate sensitivity are important for high tensile ductility since they can help prolong the elongation by delaying the necking instability. Strain rate sensitivity is related to flow stress activation volume V^* and reflects thermally activated mechanism of slip. m value of metals is usually much smaller than 1 when the quasi-static deformation occurs at room temperature [50]. The strain hardening is mainly caused by interactions between dislocations and other lattice defects as well as themselves. Therefore, the strain hardening capability is important and determines the overall tensile ductility. Refining the coarse grain (CG) down to NS and UFG regions took away the space for dislocation accumulation and multiplication, and therefore the strain hardening capability was reduced to approximately zero. This explains why the necking instability occurred immediately after yielding for the UFG/1050Al in Fig. 3. Introducing high-density nanoscale precipitates inside the UFG grains of 7075Al regained the strain hardening by further elevating dislocation accumulation capability, as shown in Fig. 3.

As stated in the introduction part, great efforts have been made to enhance the poor ductility, and more or less successes have been achieved up to now [9−23]. However, the ductility of NS and UFG materials is still not over that of the CG counterpart, i.e., the strength−ductility paradox still persists. It seems that the ductility of the CG counterpart is the extreme limit that is difficult to exceed. The bimodal and multi-modal grain size distribution solution is to compromise among the contradictory properties via combining their corresponding favorable structures together [9]. For instance, both moderate strength and ductility are achieved in bimodal and gradient nano-grained Cu alloy

because NS grains contribute to strength and CGs to ductility [27,51−53]. In fact, the compromise only makes a balance between the contradictory properties, and does not solve the contradiction from the root.

4.2 Deformation mechanisms

In the last several decades, numerous investigations of experiments, molecular dynamic (MD) simulations and other modeling efforts on deformation mechanisms of the NS and UFG materials have revealed GB-mediated deformation such as grain rotation [54], GB sliding [55], GB diffusion [56] and stress-driven GB migration [57] besides conventional slip of lattice dislocations [58]. Grain coalescence or growth usually occurs as a result of the above GB-mediated deformation [59]. Nevertheless, at room temperature, the NC and UFG materials have still exhibited significant decrease in ductility due to their poor strain hardening capability.

4.2.1 GB sliding

At elevated temperatures, GB sliding, i.e., individual grains displaced with respect to each other along their mutual boundaries as a consequence of an external stress, is a well-established deformation process for CG materials. The sliding of individual grain is accommodated either through the intra-granular dislocation slip or through the diffusional flow of vacancies [60].

The GB sliding of the NS and UFG materials has been reported to occur even at room temperature [55] because of the enhanced diffusion kinetics and/or stress-driven GB migration [57]. For the former reason, as suggested by LIDDICOAT et al in 2010 [60], even at room temperature, diffusion can play an important role in the plastic deformation of the NS and UFG metals and alloys. The increased volume fraction of GBs promotes the GB diffusion processes due to enhanced diffusivity [61]. Moreover, high fractions of high-angle GBs and non-equilibrium GBs with many extrinsic dislocations lying in narrow regions adjacent to the GBs have been frequently reported in the NS and UFG materials. These boundaries and the associated high dislocation densities are probable to provide easy diffusive paths for the local re-arrangements needed to form the GB sliding. For the latter reason, stress-driven GB migration is also revealed as an athermal activation process by some in situ TEM observations [57]. The GB sliding is even observed to occur at very low temperature, such as at liquid nitrogen temperature [62].

4.2.2 Cooperative GB sliding and micro shear bands

HAHN and PADMANABHAN [63] proposed a theoretical model for the deformation of the NS and UFG materials, i.e., the formation of mesoscopic glide planes based on the GB sliding. For the NS and UFG materials, the high volume fraction of the GBs was argued to provide an opportunity for the formation of long planar interfaces by stretching over many grains and resulting in a macroscopic sliding over individual grain dimensions. Moreover, a cooperative GB sliding of the UFG materials was observed at ambient temperatures by in situ SEM and TEM observations [56]. In addition, the above mesocopic shear planes and/or cooperative GB sliding are also revealed by MD, modeling computer simulations [64] and experiments [39]. A co-operative GB sliding of a series of the NS and UFG grains was observed in NS Fe, Cu alloys, UFGAl alloys [39,43,44], 6061Al alloys [45] and Ni alloys [46].

In CG materials, the initial dimensions of micro shear bands are significantly smaller than the coarse grain size because they are formed within a coarse grain. However, the micro shear bands of the UFG metals are different from those seen in CG materials. The micro shear bands in CG materials grow by spreading into neighboring grains across GBs and eventually form macro shear bands. Such a relationship between the grain size and the dimensions of micro shear band does not apply to the NS and UFG metals. Therefore, those shear bands in UFG metals, with width/grain size ratio in the range of 1−10, are defined as micro shear bands. They are distinct from the macro shear bands which spread across the entire specimen cross-section, form a fracture surface and result in failure.

4.3 Shear fracture

The larger shear angles than 45° in our work demonstrated that the shear fracture occurred outside the maximum shear stress plane. In fact, the shear angle is intensively affected by the fracture stress [47,48]. As illustrated by the graphic representation in Fig. 6(a), if the fracture stress σ is

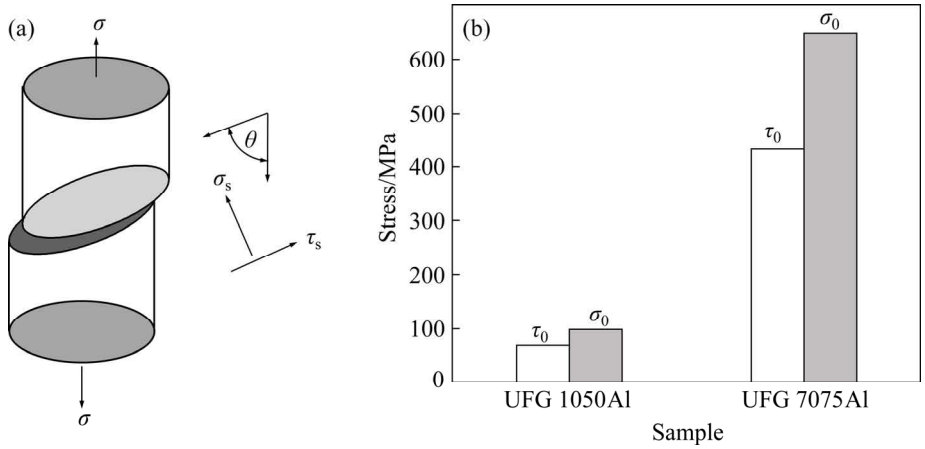

Fig. 6 Schematic representation of tensile fracture (a) and histogram of average critical normal fracture stress σ_0 and average critical shear fracture stress τ_0 for UFG 7075Al and 1050Al samples (b)

imposed on the sample, the normal and shear stresses (σ_s and τ_s, respectively) on the shear plane with a shear angle θ can be expressed as

$$\sigma_s=\sigma\sin^2\theta \tag{2}$$

$$\tau_s=\sigma\sin\theta\cos\theta \tag{3}$$

The σ, σ_s and τ_s finally determine θ. To better understand the shear angle and the shear fracture mechanism, ZHANG and ECKERT [48] proposed a unified tensile fracture criterion as follows:

$$\left(\frac{\sigma_s}{\sigma_0}\right)^2+\left(\frac{\tau_s}{\tau_0}\right)^2=1 \tag{4}$$

where σ_0 and τ_0 are the average critical normal and shear fracture stresses of a material, respectively. According to the unified tensile fracture criterion, τ_0 and σ_0 can be calculated by the following equations:

$$\sigma=2\tau_0\sqrt{1-\alpha^2} \tag{5}$$

$$\theta=\frac{\pi}{2}-\frac{1}{2}\arctan\left(\frac{\sqrt{1-2\alpha^2}}{\alpha^2}\right) \tag{6}$$

$$\alpha=\frac{\tau_0}{\sigma_0} \tag{7}$$

where the ratio α is a fracture mode factor controlling the macro-scale fracture mode of a material. It is suggested that when $0<\alpha<\sqrt{2}/2$, the shear fracture angle θ is in the range of 45°−90° [48].

According to the unified tensile fracture criterion, the ratios α of the UFG 1050Al and 7075Al samples were calculated to be 0.696 and 0.668, respectively. Their σ_0 and τ_0 were 99 MPa, 69 MPa and 648 MPa, 433 MPa, respectively. As shown in Fig. 6(b) and Table 4, σ_0 and τ_0 of the UFG 7075Al alloy are larger than those of the UFG 1050Al alloy. The proportion of σ_0 to τ_0 in the UFG 7075Al alloy is also larger than that in the UFG 1050Al alloy, resulting in a smaller ratio α and a larger shear fracture angle in the UFG 7075Al alloy. It has been demonstrated that the ECAP process can effectively change the fracture mode from normal fracture to shear fracture with different shear fracture angles [65]. The introduction of nanoscale precipitates in UFG 7075Al matrix weakened the tendency of shear fracture and make deformation more uniform, resulting in a higher tensile ductility.

Table 4 Fracture strength σ, shear fracture angle θ, fracture mode factor α, average critical normal fracture stress σ_0 and average critical shear fracture stress τ_0 of UFG 7075Al and 1050Al samples

Sample	σ/MPa	θ/(°)	α	σ_0/MPa	τ_0/MPa
1050Al	100	52	0.696	99	69
7075Al	480	58	0.668	648	433

5 Conclusions

(1) Postmortem microstructural observation revealed that, different from the GB precipitation during postmortem aging, in situ thermo-mechanical treatment made precipitation prior to GB formation, resulting in nanoscale precipitates only in the grain interiors and avoiding GB precipitation.

(2) Tensile test revealed superior mechanical properties of the UFG 7075Al alloy compared with the UFG 1050Al counterpart. The UFG 7075Al sample has the yield strength and ultimate tensile strength of 350 MPa and 500 MPa, uniform elongation of 18% and tensile ductility of 19%, respectively; while the UFG 1050Al counterpart has the yield strength and ultimate tensile strength of 170 MPa and 180 MPa, uniform elongation of 2.5% and tensile ductility of 7%, respectively.

(3) The fracture surface morphology studies revealed the activation of numerous homogeneous micro shear bands in both UFG 7075Al and 1050Al alloys, which is controlled by cooperative GB sliding. The introduction of nanoscale precipitates in UFG 7075Al matrix weakened the tendency of shear fracture and made deformation more uniform, resulting in a higher tensile ductility.

(4) This strategy may be applicable to different age hardening alloys to optimize strength and ductility by avoiding GB precipitation.

Acknowledgments

This work was supported by the National Key R&D Program of China (No. 2017YFA0204403), the National Natural Science Foundation of China (Nos. 51971112, 51225102), and the Fundamental Research Funds for the Central Universities, China (No. 30919011405).

References

[1] CAO Y, NI S, LIAO X Z, SONG M, ZHU Y T. Structure evolution of metallic materials processed by severe plastic deformation [J]. Materials Science and Engineering R, 2018, 133: 1−59.

[2] GLEITER H. Nanocrystalline materials [J]. Progress in Materials Science, 1989, 33: 223−315.

[3] MEYERS M A, MISHRA A, BENSON D J. Mechanical properties of nanocrystalline materials [J]. Progress in Materials Science, 2006, 51: 427−556.

[4] KOCH C C, MORRIS D G, LU K, INOUE A. Ductility of nanostructured materials [J]. MRS Bulletin, 1999, 24: 54−58.

[5] CHEN Xiang, HUANG Guang-sheng, LIU Shuai-shuai, HAN Ting-zhuang, JIANG Bin, TANG Ai-tao, ZHU Yun-tian, PAN Fu-sheng. Grain refinement and mechanical properties of pure aluminum processed by accumulative extrusion bonding [J]. Transactions of Nonferrous Metals Society of China, 2019, 29: 437−447.

[6] WANG Yan-fei, WANG Ming-sai, YIN Kun, HUANG Ai-hui, LI Yu-sheng, HUANG Chong-xiang. Yielding and fracture of coarse/ultrafine-grained heterogeneous-structured copper with transitional interface [J]. Transactions of Nonferrous Metals Society of China, 2019, 29: 588−594.

[7] HONG Xia, GODFREY A W, LIU Wei. Anisotropic tensile behavior and related yield point phenomena in annealed ultrafine-grained pure aluminum [J]. Transactions of Nonferrous Metals Society of China, 2018, 28: 585−591.

[8] YANG Yang, WANG Jun-ling, CHEN Ya-dong, HU Hai-bo. Effect of strain rate on microstructural evolution and thermal stability of 1050 commercial pure aluminum [J]. Transactions of Nonferrous Metals Society of China, 2018, 28: 1−8.

[9] ZHAO Y H, ZHU Y T, LAVERNIA E J. Strategies for improving tensile ductility of bulk nanostructured materials [J]. Advanced Engineering Materials, 2010, 12: 769−778.

[10] OVIKO I A, VALIEV R Z, ZHU Y T. Review on superior strength and enhanced ductility of metallic nanomaterials [J]. Progress in Materials Science, 2018, 94: 462−540.

[11] HAN B Q, LAVERNIA E J, MOHANED F A. Mechanical properties of nanostructured materials [J]. Reviews on Advanced Materials Science, 2005, 9: 1−16.

[12] ZHAO Y H, TOPPONG T, BINGERT J F, DANGELEWICZ A M, LI Y, LIU W, ZHU Y T, ZHOU Y Z, LAVERNIA E J. High tensile ductility and strength in bulk nanostructured nickel [J]. Advanced Materials, 2008, 20: 3028−3033.

[13] ZHAO Y H, LIAO X Z, CHENG S, MA E, ZHU Y T. Simultaneously increasing the ductility and strength of nanostructured alloys [J]. Advanced Materials, 2006, 18: 2280−2283.

[14] CHENG S, ZHAO Y H, ZHU Y T, MA E. Optimizing the strength and ductility of fine structured 2024 Al alloy by nano-precipitation [J]. Acta Materialia, 2007, 55: 5822−5832.

[15] LIU G, ZHANG G J, JIANG F, DING X D, SUN Y J, SUN J, MA E. Nanostructured high-strength molybdenum alloys with unprecedented tensile ductility [J]. Nature Materials, 2013, 12: 344−350.

[16] ZHAO Y H, BINGERT J F, LIAO X Z, CUI B Z, HAN K, SERGUEEVA A V, MUKHERJEE A K, VALIEV R Z, LANGDON T G, ZHU Y T. Simultaneously increasing the ductility and strength of ultra-fine grained pure copper [J]. Advanced Materials, 2006, 18: 2949−2953.

[17] CHENG S, CHOO H, ZHAO Y H, WANG X L, ZHU Y T, WANG Y D, ALMR J, LIAW P K, JIN J E, LEE Y K. High ductility of ultrafine-grained steel via phase transformation [J]. Journal of Materials Research, 2008, 23: 1578−1586.

[18] ZHAO Y H, BINGERT J F, ZHU Y T, LIAO X Z, VALIEV R Z, HORITA Z, LANGDON T G, ZHOU Y Z, LAVERNIA E J. Tougher ultrafine grain Cu via high-angle grain boundaries and low dislocation density [J]. Applied Physics Letters, 2008, 92: 081903.

[19] WANG Y M, MA E, VALIEV R Z, ZHU Y T. Tough nanostructured metals at cryogenic temperatures [J]. Advanced Materials, 2004, 16: 328−331.

[20] WANG Y M, MA E. Three strategies to achieve uniform tensile deformation in a nanostructured metal [J]. Acta Materialia, 2004, 52: 1699−1709.

[21] CHENG S, ZHAO Y H, GUO Y, WEI Q, WANG X L, REN Y, LIAW P K, CHOO H, LAVERNIA E J. High plasticity and substantial deformation in nanocrystalline NiFe alloy under dynamic loading [J]. Advanced Materials, 2009, 21:

5001−5004.

[22] WU X L, ZHU Y T. Heterogeneous materials: A new class of materials with unprecedented mechanical properties [J]. Materials Research Letters, 2017, 5: 527−532.

[23] ZHU Y T, AMEYAMA K, ANDERSON P M, BEYERLEIN I J, GAO H J, KIM H S, LAVERNIA E J, MATHAUDHU S, MUGHRABI H, RICHIE R O, TSUJI N, ZHANG X Y, WU X L. Heterostructured materials: Superior properties from hetero-zone interaction [J]. Materials Research Letters, 2021, 9: 1−31.

[24] KOCH C C. Optimization of strength and ductility in nanocrystalline and ultrafine grained metals [J]. Scripta Materialia, 2003, 49: 657−662.

[25] HORITA Z, OHASHI K, FUJITA T, KANEKO K, LANGDON T G. Achieving high strength and high ductility in precipitation-hardened alloys [J]. Advanced Materials, 2005, 17: 1599−1602.

[26] KIM W J, CHUNG C S, MA D S, HONG S I, KIM H K. Optimization of strength and ductility of 2024 Al by equal channel angular pressing (ECAP) and post-ECAP aging [J]. Scripta Materialia, 2003, 49: 333−338.

[27] KIM W J, SA Y K. Micro-extrusion of ECAP processed magnesium alloy for production of high strength magnesium micro-gears [J]. Scripta Materialia, 2006, 54: 1391−1395.

[28] SHANMUGASUNDARAM T, MURTY B S, SARMA V S. Development of ultrafine grained high strength Al−Cu alloy by cryorolling [J]. Scripta Materialia, 2006, 54: 2013−2017.

[29] TAKATA N, OHTAKE Y, KITA K, KITAGAWA K, TSUJI N. Increasing the ductility of ultrafine-grained copper alloy by introducing fine precipitates [J]. Scripta Materialia, 2009, 60: 590−593.

[30] HU C M, LAI C M, DU X H, HO N J, HUANG J C. Enhanced tensile plasticity in ultrafine-grained metallic composite fabricated by friction stir process [J]. Scripta Materialia, 2008, 59: 1163−1166.

[31] HASSEN S F, GUPTA M. Enhancing physical and mechanical properties of Mg using nanosized Al_2O_3 particulates as reinforcement [J]. Metallurgical and Materials Transactions A, 2005, 36: 2053−2258.

[32] KUWABARA T, KURISHITA H, HASGAWA M. Development of an ultra-fine grained V−1.7mass%Y alloy dispersed with yttrium compounds having superior ductility and high strength [J]. Materials Science and Engineering A, 2006, 417: 16−23.

[33] SONG R, PAGE D, RAABE D. Improvement of the work hardening rate of ultrafine grained steels through second phase particles [J]. Scripta Materialia, 2005, 52: 1075−1080.

[34] PARK K T, LEE C S, SHIN D H. Strain hardenability of ultrafine grained low carbon steels processed by ECAP [J]. Reviews on Advance Materials Science, 2005, 10: 133−137.

[35] YANG T, ZHAO Y L, TONG Y, JIAO Z B, WEI J, CAI J X, HAN X D, CHEN D, HU A, KAI J J, LU K, LIU Y, LIU C T. Multicomponent intermetallic nanoparticles and superb mechanical behaviors of complex alloys [J]. Science, 2018, 362: 933−937.

[36] LEI Z F, LIU X J, WU Y, WANG H, JIAN S H, WANG S D, HUI X D, WU Y D, GAULT B, KONTIS P, RAABE D, GU L, ZHANG Q H, CHEN H W, WANG H T, LIU J B, AN K, ZENG Q S, NIEH T G, LU Z P. Enhanced strength and ductility in a high-entropy alloy via ordered oxygen complexes [J]. Nature, 2018, 563: 546−550.

[37] WEN H M, ZHAO Y H, TOPPING T D, ASHFORD D, FLGUEIREDO R B, XU C, LANGDON T G, LAVRNIA E J. Influence of pressing temperature on microstructure evolution and mechanical behavior of ultrafine-grained Cu processed by equal-channel angular pressing [J]. Advanced Engineering Materials, 2012, 14: 185−194.

[38] SHA G, WANG Y B, LIAO X Z, DUAN Z C, RINGER S P, LANGDON T G. Influence of equal-channel angular pressing on precipitation in an Al−Zn−Mg−Cu alloy [J]. Acta Materialia, 2009, 57: 3123−3132.

[39] ZHAO Y H, BINGERT J F, TOPPING T D, SUN P L, LIAO X Z, ZHU Y T, LAVERNIA E J. Mechanical behavior, deformation mechanism and microstructure evolutions of ultrafine-grained Al during recovery via annealing [J]. Materials Science and Engineering A, 2020, 772: 138706.

[40] SHAARBAF M, TOROGHINEJAD M R. Evaluation of texture and grain size of nanograined copper produced by the accumulative roll bonding process [J]. Metallurgical and Materials Transactions A, 2009, 40: 1693−1700.

[41] ZHAO Y H, GUO Y Z, WEI Q, TROY T D, DANGELEWICZ A M, ZHU Y T, LANGDON T G, LAVERNIA E J. Influences of specimen dimensions and strain measurement methods on tensile stress−strain curves [J]. Materials Science and Engineering A, 2009, 525: 68−77.

[42] ZHAO Y H, GUO Y Z, WEI Q, DANGELEWICZ A M, ZHU Y T, LANGDON T G, LAVERNIA E J. Influence of specimen dimensions on the tensile behavior of ultrafine-grained Cu [J]. Scripta Materialia, 2008, 59: 627−630.

[43] HUANG Y, LANGDON T G. Using atomic force microscopy to evaluate the development of mesoscopic shear planes in materials processed by severe plastic deformation [J]. Materials Science and Engineering A, 2003, 358: 114−121.

[44] CHINK N Q, SZOMMER P, HORITA Z, LANGDON T G. Experimental evidence for grain-boundary sliding in ultrafine-grained aluminum processed by severe plastic deformation [J]. Advanced Materials, 2006, 18: 34−39.

[45] SABIROV I, ESTRIN Y, BARNETT M R, TIMOKHINA I, HODGSON P D. Tensile deformation of an ultrafine-grained aluminium alloy: Micro shear banding and grain boundary sliding [J]. Acta Materialia, 2008, 56: 2223−2230.

[46] VINOGRADOV A, HASHIMOTO S, PATLAN V, KITAGAWA K. Atomic force microscopic study on surface morphology of ultra-fine grained materials after tensile testing [J]. Materials Science and Engineering A, 2001, 319: 862−866.

[47] ZHANG Z F, HE G, ECKERT J, SCHULTZ L. Fracture mechanisms in bulk metallic glassy materials [J]. Physical Review Letters, 2003, 91: 045505.

[48] ZHANG Z F, ECKERT J. Unified tensile fracture criterion [J]. Physical Review Letters, 2005, 94: 094301.

[49] HART E W. Theory of the tensile test [J]. Acta Metallurgica 1967, 15: 351−355.

[50] WEI Q, CHENG S, RAMESH K T, MA E. Effect of nanocrystalline and ultrafine grain sizes on the strain rate sensitivity and activation volume: fcc versus bcc metals [J]. Materials Science and Engineering A, 2004, 381: 71−79.

[51] WANG Y M, CHEN M W, ZHOU F H, MA E. High tensile

ductility in a nanostructured metal [J]. Nature, 2002, 419: 912−914.
[52] LU K. Making strong nanomaterials ductile with gradients [J]. Science, 2014, 345: 1455−1456.
[53] FANG T H, LI W L, TAO N R, LU K. Revealing extraordinary intrinsic tensile plasticity in gradient nano-grained copper [J]. Science, 2011, 331: 1587−1590.
[54] SHAN Z W, STACH E A, WIEZOREK J M K, KNAPP J A, FOLLSTAEDT D M, MAO S X. Grain boundary-mediated plasticity in nanocrystalline nickel [J]. Science, 2004, 305: 654−657.
[55] YAMAKOV V, WOLF D, PHILLPOT S R, MUKHERJEE A K, GLEITER H. Deformation-mechanism map for nanocrystalline metals by molecular-dynamics simulation [J]. Nature Materials, 2004, 3: 43−47.
[56] SERGUEEVA A V, MARA N A, MUKHERJEE A K. Grain boundary sliding in nanomaterials at elevated temperatures [J]. Journal of Materials Science, 2007, 42: 1433−1438.
[57] RUPERT T J, GIANOLA D S, GAN Y, HEMKER K J. Experimental observations of stress-driven grain boundary migration [J]. Science, 2009, 326: 1686−1690.
[58] WANG J W, NARAYANA S, HUANG J Y, ZHANG Z, ZHU T, MAO S X. Atomic-scale dynamic process of deformation-induced stacking fault tetrahedra in gold nanocrystals [J]. Nature Communications, 2013, 4: 2340.
[59] CHENG S, ZHAO Y H, WANG Y M, LI Y, WANG X L, LIAW P K, LAVERNIA E J. Structure modulation driven by cyclic deformation in nanocrystalline NiFe [J]. Physical Review Letters, 2010, 104: 255501.
[60] LANGDON T G. An evaluation of the strain contributed by grain boundary sliding in superplasticity [J]. Materials Science and Engineering A, 1994, 174: 225−230.
[61] LIDDICOAT P V, LIAO X Z, ZHAO Y H, ZHU Y T, MURASHKIN M Y, LAVERNIA E J, RUSLAN R Z, RINGER S P. Nanostructural hierarchy increases the strength of aluminium alloys [J]. Nature Communications 2010, 1: 63.
[62] ZHANG K, WEERTMAN J R, EASTMAN J A. Rapid stress-driven grain coarsening in nanocrystalline Cu at ambient and cryogenic temperatures [J]. Applied Physical Letters, 2005, 87: 061921.
[63] HAHN H, PADMANABHAN K A. A model for the deformation of nanocrystalline materials [J]. Philosophical Magazine B, 1997, 76: 559−571.
[64] HASNAOUI A, SWYGENHOVEN H, van DERLET P M. Cooperative processes during plastic deformation in nanocrystalline fcc metals: A molecular dynamics simulation [J]. Physical Review B, 2002, 66: 184112.
[65] FANG D R, DUAN Q Q, ZHAO N Q, LI J J, WU S D, ZHANG Z F. Tensile properties and fracture mechanism of Al–Mg alloy subjected to equal channel angular pressing [J]. Materials Science and Engineering A , 2007, 459: 137−144.

采用原位热机械处理技术避免时效强化合金的晶界析出和强韧损失

赵永好

南京理工大学 材料科学与工程学院 纳米异构中心，南京 210094

摘　要：为了避免时效强化合金的晶界析出对断裂伸长率造成致命损失，提出一种原位热机械处理技术新方案。对 7075Al 合金在 250 °C 下进行 8 道次等径角挤压变形，在制备超细晶基体的同时，将高密度纳米析出相引入晶粒内部，从而避免晶界析出。拉伸实验结果表明，该超细晶 7075Al 合金具有优异的力学性能(屈服强度 350 MPa、抗拉强度 500 MPa、均匀伸长率 18%和断裂伸长率 19%)，而相应的超细晶 1050Al 合金仅具有 170 MPa 的屈服强度、180 MPa 的抗拉强度、2.5%的均匀伸长率和 7%的断裂伸长率。断口分析结果表明，超细晶 7075Al 和 1050Al 合金颈缩区的高密度微观剪切变形带由晶界集体滑动所致；超细晶 7075Al 合金中纳米析出相的引入能减弱剪切断裂的趋势，从而使塑性变形更加均匀，拉伸塑性提高。与变形处理后的时效退火不同，在原位热机械处理过程中超细晶晶界的动态形成晚于晶内纳米析出，从而避免晶界析出。

关键词：时效强化合金；强度；断裂伸长率；晶界析出；原位热机械处理技术

(Edited by Wei-ping CHEN)